Hindawi Publishing Corporation
Journal of Nanomaterials
Volume 2013, Article ID 265797, 9 pages
http://dx.doi.org/10.1155/2013/265797

Research Article

Effect of Calcination Temperature on Structural Properties and Photocatalytic Activity of Ceria Nanoparticles Synthesized Employing Chitosan as Template

Angela B. Sifontes,[1] Maibelin Rosales,[2] Franklin J. Méndez,[1] Olycen Oviedo,[2] and Tamara Zoltan[2]

[1] *Laboratorio de Físico-Química de Superficies, Centro de Química, Instituto Venezolano de Investigaciones Científicas I.V.I.C., Caracas 1020-A, Venezuela*
[2] *Laboratorio de Fotoquímica, Centro de Química, Instituto Venezolano de Investigaciones Científicas I.V.I.C., Caracas 1020-A, Venezuela*

Correspondence should be addressed to Tamara Zoltan; tzoltan@ivic.gob.ve

Received 11 April 2013; Accepted 22 May 2013

Academic Editor: Suprakas Sinha Ray

Ceria nanoparticles were synthesized employing chitosan as template and thermal treatment at different temperatures (350, 650, and 960°C). The effect of calcination temperature on structural properties and photocatalytic activity of ceria nanopowder was also tested. Degradation of an azo dye, Congo Red (CR) as a model aqueous pollutant, was investigated by means of photocatalysis of ceria nanoparticles under visible light irradiation. The influence of catalyst amount, initial CR concentrations, and degradation reaction kinetics were studied. The results were compared with commercial CeO_2 at the same degradation conditions.

1. Introduction

The application of heterogeneous semiconductor photocatalysts in water treatment has recently drawn considerable attention because of the successful use of solar energy, which is a natural abundant energy source [1]. Of all semiconductor photocatalysts employed in water purification, TiO_2, with a bandgap energy of 3.2 eV, was found to exhibit high photocatalytic activity under UV light irradiation. Besides the most commonly used TiO_2 catalyst, cubic fluorite cerium dioxide (CeO_2), a semiconductor with a bandgap energy similar to that of titania, [2] also shows promising photocatalytic activity for the degradation of various organic dye pollutants such as Methylene Blue (MB), Methyl Orange (MO), and Reactive Black 5 (RB5). CeO_2 has also been successfully employed in water splitting for H_2 production and phenol and chlorinated phenol photodegradation under UV illumination. Although photocatalytic activity of CeO_2 has thoroughly been investigated, the broad bandgap energy of this material limits its further application in the visible light region. In this regard, many methodologies have been carried out for the modification of CeO_2, in order to enhance its photocatalytic activity in the visible region: doping with metals and preparation of composite materials, among others. Nonetheless, so far there are no reports of increased photoactivity in the visible region, changing their morphology through calcination temperature.

Photocatalytic properties of the materials are primarily dependent on various factors such as particle size, phase modification, structural defects/distortion (lattice), and chemical nonstoichiometry [3]. Commonly, reducing the particle size of a catalyst results in an increase of the surface area and changing its morphology, thus providing a larger number of reactive edge sites [4, 5]. It has been reported that, in general, an increase in the temperature of calcination provides a high crystallinity [6], a decrease in the surface area [7] and, for mixed materials or doped semiconductors, an absorption shift toward the visible spectrum [8, 9]. In this

sense, it has been reported that the direct relationship that exists between great surface areas and high catalytic efficiency is not always fulfilled in photocatalytic materials [10]. The justification for such behavior is based on that the energy absorption processes and the subsequent migration of electrons in the valence band (and recombination) are not simply a result of physical adsorption phenomena in the material surface. In this way, you can see that a detailed study of the electronic and morphological characteristics of new synthetic materials provide information about their potential use as photocatalysts.

Crystalline ceria nanoparticles can be synthesized by different methods, such as sonochemical [11], thermal decomposition [12] hydrothermal synthesis [13], coprecipitation [14], flame spray pyrolysis [15], combustion synthesis, and solvothermal oxidation [16]. These methodologies often require high pressure, or salt-solvent mediated high temperature, or surface capping agent. Moreover, the introduction of surfactants or templates complicated the manufacture, consumed more energy, and was not environmental friendly [17]. In addition, the sizes obtained of ceria particles are relatively large [18]. Therefore, the search for alternatives that allow the productions of cerium nanoparticles using "green" pathways, simple and low cost, is essential.

Dyes and pigments represent one problematic group; they are emitted into wastewaters from various industrial branches, mainly from the dye manufacturing and textile finishing and also from food colouring, cosmetics, paper, and carpet industries [19]. Congo red [1-naphthalene sulfonic acid, 3, 30-(4,40-biphenylenebis (azo)) bis (4-amino-) disodium salt, CR: Figure 1] is a benzidine-based anionic diazo dye, that is, a dye with two azo groups. CR is toxic to organisms and it is a suspected carcinogen and mutagen. Synthetic dyes, such as CR, are difficult to biodegrade due to their complex aromatic structures, which provide them physicochemical, thermal, and optical stability [20, 21]. Physicochemical or chemical treatment of such wastewaters is, however, possible: color removal by ultrafiltration [22], ozonation [23], coagulation [24], adsorption process [18], and so forth. The use of Advanced Oxidation Processes (AOPs), photochemically induced employing pure semiconductors [25], mixed or sensitized [26], has been widely used in recent years for the efficient degradation of CR.

Therefore, it is important to find alternatives to the degradation of reactive azo dyes in an aqueous solution and destruction of several classes of organic dyes. Most conventional treatment processes are effective in water treatment, but they only transfer the contaminants from one medium to another or generate waste that requires further treatment and disposal [19–21]. In this sense, photocatalytic reactions on irradiated semiconductor powders have a good potential for the removal of organic and inorganic waste materials from water [27]. The aim of this work was to use a prepared CeO_2 nanoparticles, through a simple synthetic method, environmentally benign, and low cost using chitosan as template, Ammonium Cerium (IV) Nitrate $[(NH_4)_2Ce(NO_3)_6]$ and ammonium hydroxide [28]. Furthermore, the effect of calcination temperature of the synthesized material on size, morphology, as well as in optical properties, and the photocatalytic efficiency of the degradation of CR dissolved in water was evaluated.

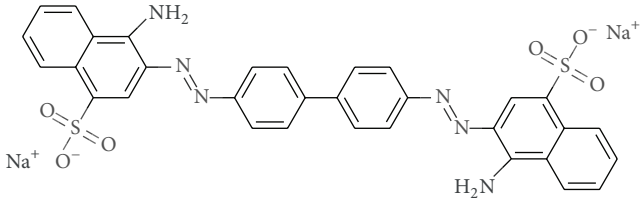

Figure 1: Molecular structure of Congo Red.

2. Experimental

2.1. Reagents and Materials. Cerium salt compound: $(NH_4)_2Ce(NO_3)_6$ (Sigma-Aldrich, purity ≥ 98.5%), Chitosan (Sigma-Aldrich, purity ≥ 99%), and NH_4OH (Sigma-Aldrich, 28.0–30.0% NH_3) were used as the starting materials. Congo Red (purity ≥ 97.0%), Acetic Acid (purity ≥ 99.7%), and $BaSO_4$ (purity > 99.99%) were purchase for Sigma-Aldrich and were used without further purification.

2.2. Synthesis and Characterization of Photocatalysts. Ceria nanoparticles were prepared using chitosan as template and a precursor Ce salt compound. Preparation was carried out following the procedure described by our group [28]. 1.6 g of chitosan was dissolved in 80 mL of CH_3COOH (3%, v/v) and 10.41 g of $(NH_4)_2Ce(NO_3)_6$ was dissolved in 20 mL of distilled water. The cerium aqueous solution was added to the chitosan solution, under stirring and this Ce-chitosan solution was added to a NH_4OH solution (50%, v/v). The gel spheres formed were taken out from NH_4OH solution and dried at room temperature for 96 h. The ceria hybrid spheres were calcined at 350, 650, and 960°C in air flow for 6 h with a heating rate of 5°C/min, to obtain light yellow CeO_2 nanoparticles.

The textural properties of the metal oxides were characterized by N_2 adsorption porosimetry (Micromeritics, ASAP 2010). The samples were first degassed at 300°C under vacuum for more than 24 h until the sample passed the degassing test. Nitrogen adsorption isotherms were measured at liquid N_2 temperature (77 K) and N_2 pressures ranging from 10^{-6} to 1.0 P/P_o. Surface areas were calculated according to Brunauer-Emmett-Teller (BET) method and the pore size distribution was obtained according to the Barret-Joyner-Halenda (BJH) method from the adsorption data [30].

The morphology and average diameter of particles were examined employing a Scanning Electron Microscopy Hitachi S-2400 instrument. The evaluation by transmission electron microscopy was performed on a Hitachi CM-10 instrument operated at 120 kV.

All the samples were characterized by diffuse reflectance spectroscopy (DRS). UV-Vis DR spectra were recorded at room temperature in the range of 200–700 nm employing a Lambda 35 UV-Vis spectrophotometer (Perkin Elmer) equipped with an integrating sphere assembly, using $BaSO_4$

as the reflectance reference sample. The absorption spectra were obtained by analyzing the reflectance measurement with Kubelka-Munk (KM) emission function: $F(R_\infty)$. Optical bandgap energy (E_g) can be determined from the plot between $E = 1240/\lambda_{Abs}$ and $[F(R_\infty)h\nu]^{1/2}$ where E is the photonic energy in eV and $h\nu$ is the energy of an incident photon.

2.3. Photocatalytic Activity for the Degradation of Congo Red (CR). The photocatalytic activities of the catalysts were evaluated by degradation of CR in aqueous solution. The photocatalysis experiments were performed in a batch reactor using an illuminator Cole Palmer 41720-series, with an emission maximum in UV 350–500 nm (3.5 mW/cm^2, 49.400 Lux/seg), keeping a distance of 10 cm between the lamp surface and the solution, varying the time periods of exposure at 25°C under continuous shaking. In a typical experiment, the reaction suspension consisting of CR aqueous solution (50 mg L^{-1}, 100 mL) and catalyst (0.05 g) was stirred with a magnetic bar. In all cases, the mixture was kept in the dark for 24 h to ensure that the adsorption-desorption equilibrium was reached before irradiation. After light irradiation, the sample was withdrawn from the suspensions every 10 min during the irradiation; 0.5 mL of the analytical solution was taken from the mixture and immediately centrifuged. The concentration of the RC in the analytical solution was determined spectrophotometrically at 498 nm. A calibration plot based on Beer-Lambert's law was established by relating the absorbance to the concentration.

3. Results and Discussion

X-ray diffraction (XRD) and transmission electron microscopy (TEM) were used to study the microstructure of metal oxides. Both techniques revealed the crystalline character of the CeO_2 powder, showing broad diffraction peaks (XRD) and diffraction rings (TEM) that are the characteristic patterns of nanocrystalline materials.

The XRD patterns of the as-prepared powder and heat-treated ceria nanoparticles at different temperatures (350, 650, and 960°C) are shown in Figure 2. The calcined samples exhibit XRD peaks that correspond to the (111), (200), (220), (311), (222), and (400) planes, which revealed well-developed reflections of cerium oxide (ICDD PDF No. 81-0792), space group *Fm*3*m* (225), showing that the synthesized samples were pure CeO_2 with cubic fluorite structure [16]. No peak of any other phase was detected. The intensities and positions of the diffraction peaks were in agreement with the literature data.

The lattice parameter of cerium oxide nanoparticles was measured using X-ray diffraction (XRD) (Table 1). The constant "*a*" of the cubic fluorite-type CeO_2 grains can be determined through the spacing of the *hkl* lattice planes (d_{hkl}) and taking into account Bragg's law [31]. The results were checked with Celref software.

SEM and TEM analysis allowed us to investigate the morphology and structure of the synthetic materials.

Ceria materials were produced by the calcination of precipitates (hybrid spheres) at 350, 650, and 960°C. SEM and TEM micrographs of calcinated materials are show in Figure 3; it can observed that the particles synthesized show the topography of foams with high porosity.

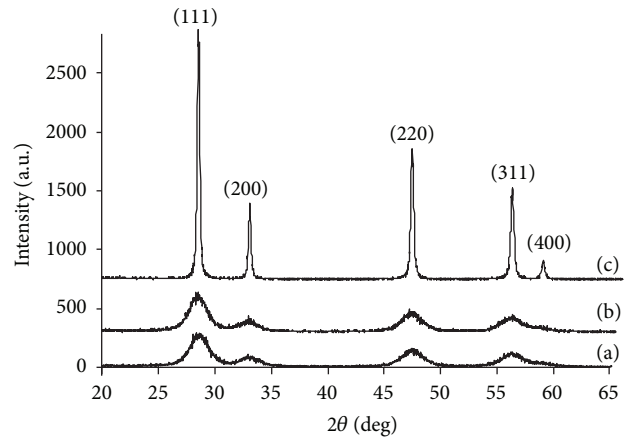

Figure 2: XRD patterns of synthesized CeO_2 nanoparticles prepared at different calcination temperatures, (a) 350°C, (b) 650°C, and (c) 960°C.

Table 1: Summary of crystallite size and lattice parameter for CeO_2 particles prepared at different calcination temperature.

Temperature (°C)	Lattice parameter (nm)	TEM crystallite size (nm)	S_{BET} (m^2/g)
350	0.5470	4	105.12
650	0.5424	17	13.02
960	0.5411	61	8.02

Figure 3 also shows TEM images with corresponding selected area electron diffraction pattern (SAED). The crystalline size has been directly estimated using such images. It can also be observed that calcined nanoparticles exhibited roughly spherical shape. Moreover, an increase in the calcination temperature led to the appreciable growth in the crystallite size.

The SAED pattern shows continuous ring patterns without any additional diffraction spots and rings of secondary phases, revealing their highly crystalline structure. As summarized in Table 2, measured interplanar spacings (d_{hkl}) from SAED patterns are in good agreement with the values in the standard data (JCPDS: 34-0394). All the rings could be precisely indexed to the cubic CeO_2 phase; this observation is in agreement with XRD results. The diffraction pattern was further examined for all possible forms of cerium oxide for matches to the unknown ring.

Surface physical properties including pore characteristics, surface area, surface morphology, and textural aspects of synthetized materials have been studied and the results are summarized in Table 3.

The data summarized in Table 3 clearly shows the formation of mesopores in the cerium nanoparticles synthesized through use of chitosan template. Furthermore, it was found that the surface area decreased with increasing calcination temperature, showing phase sintering cerium oxide with

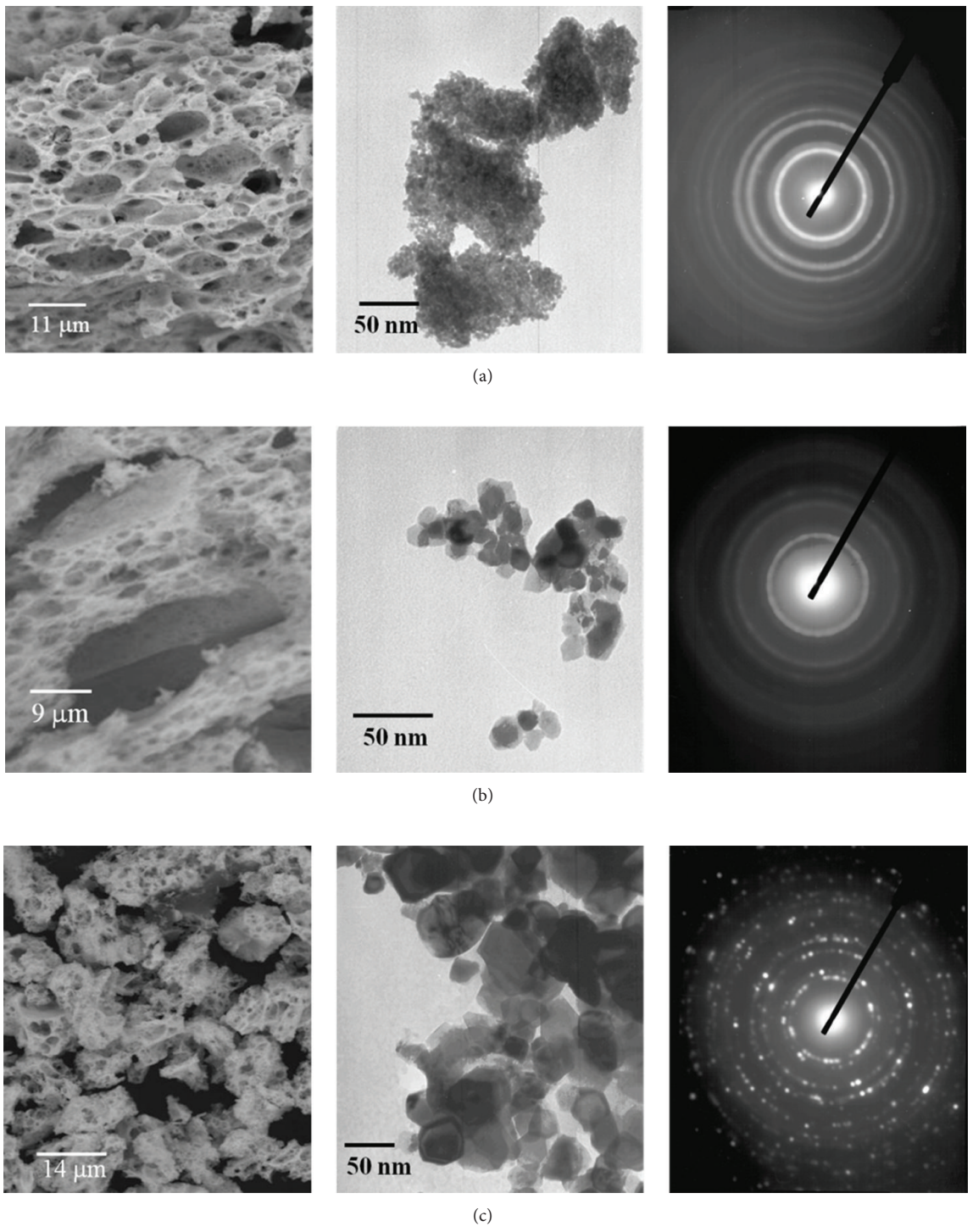

Figure 3: SEM, TEM, and electron diffraction pattern of CeO_2 nanoparticles at different calcination temperatures, (a) 350°C, (b) 650°C, and (c) 960°C.

increased high temperature crystallinity. Thus, the use of the chitosan template clearly results in a substantial increase in the surface area, and hence, the present method provides a synthesis method of easy and low cost for obtaining nanoparticles of cerium with high surface area and mesoporous.

4. UV-Vis Diffuse Reflectance Analysis

UV-vis diffuse reflectance spectroscopy (UV-vis DRS) was used to probe the band structure or molecular energy levels in the materials since UV-vis light excitation creates

Table 2: Measured interplanar spacing (d) from selected area diffraction pattern in Figure 3, compared with reference values (standard data JCPDS: 34-0394) of different cerium oxide forms.

Calcined sample CeO_2 (Å)			Standard data JCPDS: 34-0394 (Å)				
350°C	650°C	960°C	CeO_2	CeO	CeO_{2-x}	Ce_2O_3	Ce
3.119	3.099	3.124	3.124 (111)	2.938 (111)	3.39 (222)	2.945 (0111)	2.97 (111)
2.696	2.687	2.705	2.706 (200)	2.544 (200)	2.06 (044)	2.254 (1012)	2.57 (200)
1.917	1.904	1.913	1.913 (220)	1.799 (220)	1.65 (543)	1.945 (1120)	1.82 (220)
1.632	1.623	1.631	1.632 (311)	1.534 (311)		1.733 (1013)	1.55 (311)
1.562	1.556	1.561	1.561 (222)			1.637 (1122)	

Table 3: Summary of the surface are, pore diameter, and pore volume for CeO_2 materials prepared at different calcination temperature.

Temperatures (°C)	S_{BET} (m^2/g)	Pore volume (cm^3/g)	Pore diameter (nm)
350	105.12	0.065	7
650	13.02	0.023	13
960	8.02	0.020	15

photogenerated electrons and holes [32]. The DRS spectra of CeO_2 powders calcined at different temperatures (350, 650, and 960°C) are shown in Figure 4. DRS measurements were used to obtain information about absorption spectra and bandgap of catalysts or map the electronic structure of the metal ions by measuring d–d, f–d transitions, and oxygen-metal ion charge transfer bands. It has been reported that bulk CeO_2 show absorption maxima around 300 nm in its DRS [33].

According to Bensalem et al. [34], the spacing of the electronic levels and the energy bandgap (E_g) is highly dependent on the particle size. An UV absorption edge at about 500 nm occurs for ceria caused by $Ce^{+4} \leftarrow O^{2-}$ charge transfer [33–35]. When CeO_2 is synthesized at increasing calcination temperatures, a blue shift from 500 nm to 411, 375, and 364 nm is observed (respectively, for 350, 650, and 960°C). For the samples calcined this shift of the absorbance towards shorter wavelengths can be explained as a consequence of either the quantum size effect originated by the diminution of ceria particle size, or the existence of larger contribution of $Ce^{+4} \leftarrow O^{2-}$ charge transfer transitions, which yields a relatively broad band with a maximum at ca. 380 nm [33–35]. However, the calculations for the quantum size effect establish that there are no significant variations in the chemical composition in the structure of metal oxide as a result of particle size reduction [36]. In our case, the influence due to the presence of different states of oxidation of CeO_2, the presence of a significant fraction of Ce atoms (either in the state +3 or +4) on the outer surface which generates oxygen vacancies and defects, has a higher influence on the E_g, expected by quantum size effect. In this sense, the presence of Ce^{+3} species has been verified using EPR and Raman analysis. Neto and Schmal [37] show that increases in the calcination temperature, as well as in the synthesis condition, leads to an increase in the concentration of Ce^{+3} species and therefore an increase in oxygen vacancies.

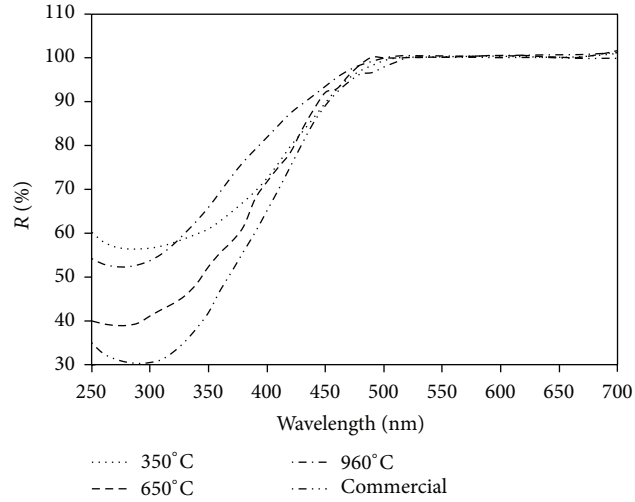

Figure 4: UV-vis diffuse reflectance spectra of CeO_2 samples after calcination at 350°C (· · ·), 650°C (- - -), and 960°C (· - ·) and commercial (·· - ··).

The E_g of synthetized samples in this work was calculated by Kubelka-Munk function $F(R)$ which is related to the diffuse reflectance, R, of the sample according to the following equation [38]:

$$F(R) = \frac{(1-R)^2}{2R}, \quad (1)$$

where "R" is the absolute value of reflectance. The E_g of the CeO_2 nanoparticles were calculated from their diffuse-reflectance spectra by plotting the square of the Kubelka-Munk function $F(R)^2$ versus energy in electron volts (Figure 5). The linear region of the curve was extrapolated to $F(R)^2 = 0$ to get the direct E_g. The optical bandgap for all samples were determined by the above method. The E_g and calculated absorption maxima of calcinated samples are given in Table 4.

Table 4 clearly shows an increase in E_g (decrease in the absorption edge) due to the increase in the crystal size. It is reported that CeO_2 nanocrystals show a bandgap energy (E_g) between 2.7 and 3.4 eV and absorb strongly in the UV region with the absorption threshold near to 400 nm (25 000 cm^{-1}). As shown in Table 4, the bandgap energies for samples calcined at different temperatures were 3.02, 3.31, and 3.41 eV for 350, 650, and 960°C, respectively.

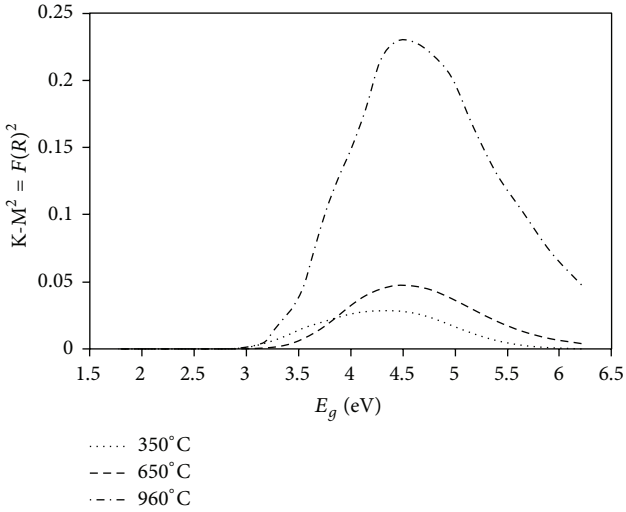

Figure 5: Bandgap measurements of CeO_2 samples after calcination at 350°C (· · ·), 650°C (- - -), and 960°C (· - ·).

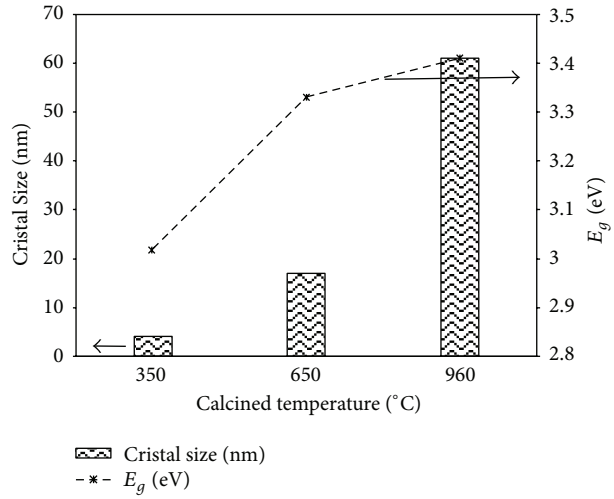

Figure 6: Correlation among the crystal size and the energy bandgap of CeO_2 samples after calcination at 350°C, 650°C, and 960°C.

Table 4: The band gap energy and crystal size of CeO_2 samples calcined at different temperatures.

Temperature (°C)	E_g (eV)	Absorption edge (nm)	Crystallite size (nm)
350	3.02	411.4	4
650	3.31	373.3	17
960	3.41	364.3	61
Commercial	3.19*	389.4	—

*Reported [29].

It can be seen that the value obtained in this work for the E_g value for the sample calcined at 350°C is lower than that reported by us previously [28]. This behavior can be explained in terms of the measurement system in the first report that the E_g was calculated from the spectrum of UV-vis absorption, whereas in this study DRS spectrum was used. In the literature, different E_g values have been found for nanoparticles of similar sizes when using different measurement systems [29, 39]. This is attributed to the fact that diffuse reflectance spectroscopy (DRS) takes advantage of the enhanced scattering phenomenon in powder materials, making this technique more suitable to characterize nanomaterials than UV-vis absorption spectroscopy. Consequently, light scattering effects in the absorption spectra of powder samples dispersed in liquid media can be avoided using DRS. [40].

The relationship between the crystal size and the bandgap energy is shown in Figure 6.

The E_g of CeO_2 is usually reported to be higher with lowering of particle size, owing to the quantum confinement effect [41]. However, the ceria samples synthesized in this work using chitosan as a template showed the opposite behavior. This could be due to formation of larger size agglomerates, feasibly as a consequence of the use of chitosan as template. Previous reports make mention of the lower bandgap energy E_g for CeO_2 nanorods as compared to that of CeO_2 nanoparticles as well, indicating the influence of crystallite size as well as the overall particle size on bandgap energy [29]. However, the incorporation of nonmetals, carbon, and nitrogen (from chitosan) in the ceria structure could also contribute to the lowering of bandgap. Heating rates in the calcination would also contribute to the presence of these elements (C and N).

5. Photocatalytic Activity

The photocatalytic activity of the CeO_2 samples calcined at different temperatures was evaluated by the photodegradation of CR at room temperature under UV and visible light irradiation. The efficiency of the materials synthesized in the photodegradation (%D) of CR was determined using the following expression [42]:

$$\%D = \frac{C_0 - C}{C_0} \times 100, \quad (2)$$

where C_0 is the initial concentration of CR and C is the remaining concentration of CR after irradiation in the desired time interval.

Figure 7 clearly shows that irradiation in the presence of CeO_2 nanoparticles leads to an increase in the degradation efficiency of CR. Materials prepared in this work all have an onset of absorption at wavelengths below 420 nm. Therefore, radiation of wavelength less than 420 nm is suitable for the transfer of electrons from the valance band to the conductance band. It can be seen that the rate of CR photodegradation increased gradually with time, reaching efficiency values of 41, 51, and 64% after 15 h to calcinated temperatures samples: 350, 650 and 960 respectively. After 24 hours of irradiation was obtained 62, 71, and 91% degradation for the samples calcined at 350, 650, and 960°C respectively, showing that higher calcination temperatures lead to higher efficiencies in the photodegradation of RC.

The photocatalytic efficiency (activity) of each CeO_2 catalyst for the degradation of Congo Red was quantified in two

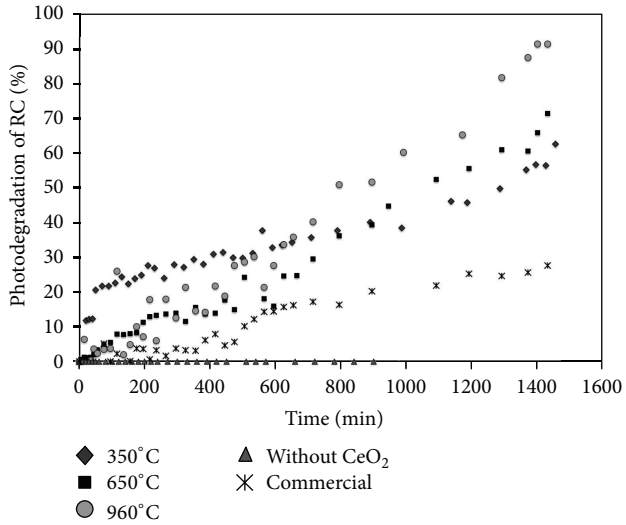

Figure 7: Degradation efficiency of CR (50 mg/L) catalyzed by CeO_2 nanoparticles (0.5 g/L) calcined at different temperatures: 350°C, 650°C, and 960°C and commercial.

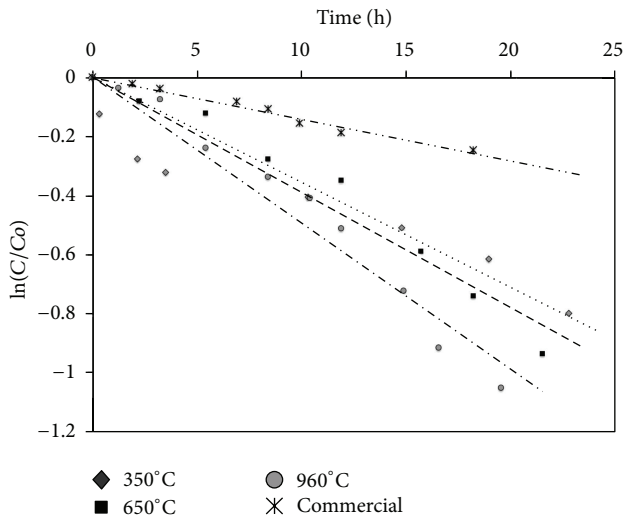

Figure 8: Apparent first order kinetic model for CR photodegradation by CeO_2 samples after calcination at 350°C (· · ·), 650°C (- - -), and 960°C (· - ·) and commercial (·· - ··), with a reaction time of 22 h.

ways: measurement of Congo Red half-life time under standard conditions and Langmuir-Hinshelwood kinetic analysis.

Surface catalyzed reactions can often be adequately described by a unimolecular Langmuir-Hinshelwood (L-H) mechanism, in which an adsorbed reactant with fractional surface coverage θ is consumed at an initial rate given by

$$r = -\frac{dC}{dt} = k_r\theta = \frac{k_r K_{LH} C}{1 + K_{LH}C + K_w C_w}, \quad (3)$$

where r is the oxidation rate of the reactant (mg L^{-1} min^{-1}), C the concentration of the reactant (mg L^{-1}), t the illumination time, k_r the constant of reaction rate (mg L^{-1} min^{-1}), K_{LH} the adsorption constant of the reactant (L mg^{-1}), K_w the solvent adsorption constant, and C_w its concentration. As $C_w \gg C$ and C_w remains practically constant, the part of the catalyst covered by water is unalterable over the whole range of concentration. In this work, all experimental conditions were the same. Therefore, C will only be variable in the initial reactions:

$$r = -\frac{dC}{dt} = \frac{k_r K_{LH} C}{1 + K_{LH}C}. \quad (4)$$

When the chemical concentration C_i is a millimolar solution (C_0 small) the equation can be simplified to an apparent first-order equation:

$$\ln\left(\frac{C}{C_0}\right) = k_r K t = -k_{app} t, \quad (5)$$

where k_{app} is the apparent pseudo-first-order reaction rate constant and t is the reaction time. The variation in the $\ln(C/C_0)$ as a function of the irradiation time t is given in Figure 8.

The straight lines obtained by plotting $\ln(C_0/C)$ versus time of irradiation indicate that the degradation of Congo Red satisfactorily fits the model L-H. This behavior allows to infer about the existence of an equilibrium between the phenomena of adsorption and photodegradation reactions. The kinetic data obtained in Figure 8 regarding to the pseudo-first-order rate constant, k_{app}, and the half-life, $t_{1/2}$, for the photocatalytic degradation of RC are listed in Table 5.

From Table 5 it can be seen that an increase in the calcination temperature leads to an increase in the rate of photodegradation of CR by cerium nanoparticles. This increase in the activity can be explained in terms of the morphological differences among the synthesized materials, since it has been reported that the photocatalytic activity of metal oxides is strongly dependent on their morphological properties [42]. Table 3 shows that the calcined material at 960 presents a greater crystallinity and particle size in comparison with the materials calcined at 350 to 650 and taking into account that a greater crystallinity of the material gives less surface defects which can act as recombination centers of electron-hole pair, explains the fact most photocatalytic activity of the calcined material at high temperatures [43]. This may be corroborated considering the low reaction rate of the commercial cerium that has a low crystallinity.

Some semiconductor materials, such as titania, it has been reported that the specific surface area and crystallinity are two contradictory factors that influence the photocatalytic activity. In that sense, amorphous semiconductor material with high surface area is generally associated with a large amount of crystal defects or weak crystallization, which favors recombination processes of electrons and holes photogenerated, causing a poor photoactivity [44]. Therefore, a large surface area is required, but not a decisive factor. For example, amorphous TiO_2 powders generally exhibit a large specific surface area, but poor photocatalytic activity or negligible due to recombination of electrons and positive holes photoexcited defects (i.e., imperfections, impurities, dangling

Table 5: Apparent constant and half-life for the Langmuir-Hinshelwood model and specific photoactivity for Congo Red photodegradation by CeO_2 nanoparticles calcined at different temperatures.

Temperature (°C)	k_{app} (h^{-1})	$t_{1/2}$ (h)	Specific photoactivity k_{app}/S_{BET} ($\bar{k}$ in g m^{-2} h^{-1})
350	0.0356	19.47	0.34×10^{-3}
650	0.0390	17.77	2.99×10^{-3}
960	0.0495	14.00	6.17×10^{-3}
Commercial	0.0141	49.16	—

bonds, or microvoids) located on the surface and in the bulk of the particles [9]. In this regard, examining the values obtained for specific photocatalytic activity (Table 5) can be seen that a high crystallinity provides higher photocatalytic activity, indicating that the crystallinity is another important requirement that must be taken into account in the design (and study) of new photocatalytic materials.

6. Conclusion

In summary, in this work cerium oxide nanoparticles using chitosan as template were synthesized and characterized. After subsequent heat treatment, an increase in degree in crystallinity and the particle size was observed as a result of temperature increase. DRS studies showed that an increase in the calcination temperature produces a blue shift in the absorption maxima of the absorption spectrum and a decrease of E_g being a consequence of the increase in particle size. Studies on the photocatalytic degradation of CR demonstrated that the calcined materials at higher temperatures, exhibited greater activity as a result of larger particle size and high crystallinity. Thus, we can conclude that variation by calcination temperatures allows obtaining materials with optical and morphological properties that enable their efficient use as photocatalysts.

References

[1] N. Wetchakun, S. Chaiwichain, B. Inceesungvorn et al., "$BiVO_4$/CeO_2 nanocomposites with high visible-light-induced photocatalytic activity," *ACS Applied Materials and Interfaces*, vol. 4, no. 7, pp. 3718–3723, 2012.

[2] G. Magesh, B. Viswanathan, R. P. Viswanath, and T. K. Varadarajan, "Photocatalytic behavior of CeO_2-TiO_2 system for the degradation of methylene blue," *Indian Journal of Chemistry A*, vol. 48, no. 4, pp. 480–488, 2009.

[3] F. Zhang, S.-W. Chan, J. E. Spanier et al., "Cerium oxide nanoparticles: size-selective formation and structure analysis," *Applied Physics Letters*, vol. 80, no. 1, pp. 127–129, 2002.

[4] B. M. Reddy and A. Khan, "Nanosized CeO_2-SiO_2, CeO_2-TiO_2, and CeO_2-ZrO_2 mixed oxides: influence of supporting oxide on thermal stability and oxygen storage properties of ceria," *Catalysis Surveys from Asia*, vol. 9, no. 3, pp. 155–171, 2005.

[5] S. Deshpande, S. Patil, S. V. Kuchibhatla, and S. Seal, "Size dependency variation in lattice parameter and valency states in nanocrystalline cerium oxide," *Applied Physics Letters*, vol. 87, no. 13, Article ID 133113, pp. 1–3, 2005.

[6] S. Mozia, "Application of temperature modified titanate nanotubes for removal of an azo dye from water in a hybrid photocatalysis-MD process," *Catalysis Today*, vol. 156, no. 3-4, pp. 198–207, 2010.

[7] A. Bumajdad, M. I. Zaki, J. Eastoe, and L. Pasupulety, "Microemulsion-based synthesis of CeO_2 powders with high surface area and high-temperature stabilities," *Langmuir*, vol. 20, no. 25, pp. 11223–11233, 2004.

[8] Y. Yang and C. Tian, "Effects of calcining temperature on photocatalytic activity of Fe-doped sulfated titania," *Photochemistry and Photobiology*, vol. 88, no. 4, pp. 816–823, 2012.

[9] J. Fan, L. Zhao, J. Yu, and G. Liu, "The effect of calcination temperature on the microstructure and photocatalytic activity of TiO_2-based composite nanotubes prepared by an in situ template dissolution method," *Nanoscale*, vol. 4, no. 20, pp. 6597–6603, 2012.

[10] J. Yu, W. Wang, B. Cheng, B. Huang, and X. Zhang, "Preparation and photocatalytic activity of multi-modally macro/mesoporous titania," *Research on Chemical Intermediates*, vol. 35, no. 6-7, pp. 653–665, 2009.

[11] R.-J. Qi, Y.-J. Zhu, G.-F. Cheng, and Y.-H. Huang, "Sonochemical synthesis of single-crystalline $CeOHCO_3$ rods and their thermal conversion to CeO_2 rods," *Nanotechnology*, vol. 16, no. 11, pp. 2502–2506, 2005.

[12] M. A. Gabal, S. A. K. Elroby, and A. Y. Obaid, "Synthesis and characterization of nano-sized ceria powder via oxalate decomposition route," *Powder Technology*, vol. 229, pp. 112–118, 2012.

[13] C. Liu, L. Luo, and X. Lu, "Preparation of mesoporous $Ce_{1-x}Fe_xO_2$ mixed oxides and their catalytic properties in methane combustion," *Kinetics and Catalysis*, vol. 49, no. 5, pp. 676–681, 2008.

[14] M. Jalilpour and M. Fathalilou, "Effect of aging time and calcination temperature on the cerium oxide nanoparticles synthesis via reverse co-precipitation method," *International Journal of the Physical Sciences*, vol. 7, no. 6, 2012.

[15] C. Chaisuk, A. Wehatoranawee, S. Preampiyawat, S. Netiphat, A. Shotipruk, and O. Mekasuwandumrong, "Preparation and characterization of CeO_2/TiO_2 nanoparticles by flame spray pyrolysis," *Ceramics International*, vol. 37, no. 5, pp. 1459–1463, 2011.

[16] M. Zawadzki, "Preparation and characterization of ceria nanoparticles by microwave-assisted solvothermal process," *Journal of Alloys and Compounds*, vol. 454, no. 1-2, pp. 347–351, 2008.

[17] M. Sun, G. Zou, S. Xu, and X. Wang, "Nonaqueous synthesis, characterization and catalytic activity of ceria nanorods," *Materials Chemistry and Physics*, vol. 134, no. 2-3, pp. 912–920, 2012.

[18] S. Kaur, S. Rani, and R. K. Mahajan, "Adsorption kinetics for the removal of hazardous dye congo red by biowaste materials as adsorbents," *Journal of Chemistry*, vol. 2013, Article ID 628582, 12 pages, 2013.

[19] I. D. Mall, V. C. Srivastava, N. K. Agarwal, and I. M. Mishra, "Removal of congo red from aqueous solution by bagasse fly ash and activated carbon: kinetic study and equilibrium isotherm analyses," *Chemosphere*, vol. 61, no. 4, pp. 492–501, 2005.

[20] S. P. Meshram, D. T. Tayade, P. D. Ingle, P. D. Jolhe, B. B. Diwate, and S. B. Biswas, "Ultrasonic cavitation induced degradation of Congo red in aqueous solutions," *Chemical Engineering Research Bulletin*, vol. 14, no. 2, 2010.

[21] H. Chen and J. Zhao, "Adsorption study for removal of Congo red anionic dye using organo-attapulgite," *Adsorption*, vol. 15, no. 4, pp. 381–389, 2009.

[22] H. P. Srivastava, G. Arthanareeswaran, N. Anantharaman, and V. M. Starov, "Performance of modified poly(vinylidene fluoride) membrane for textile wastewater ultrafiltration," *Desalination*, vol. 282, pp. 87–94, 2011.

[23] P. Gharbani, S. M. Tabatabaii, and A. Mehrizad, "Removal of Congo red from textile wastewater by ozonation," *International Journal of Environmental Science and Technology*, vol. 5, no. 4, pp. 495–500, 2008.

[24] S. M. Tsui and W. Chu, "Quantum yield study of the photodegradation of hydrophobic dyes in the presence of acetone sensitizer," *Chemosphere*, vol. 44, no. 1, pp. 17–22, 2001.

[25] J. Wang, Y. Guo, B. Liu et al., "Detection and analysis of reactive oxygen species (ROS) generated by nano-sized TiO_2 powder under ultrasonic irradiation and application in sonocatalytic degradation of organic dyes," *Ultrasonics Sonochemistry*, vol. 18, no. 1, pp. 177–183, 2011.

[26] H. Zhu, R. Jiang, L. Xiao et al., "Photocatalytic decolorization and degradation of Congo Red on innovative crosslinked chitosan/nano-CdS composite catalyst under visible light irradiation," *Journal of Hazardous Materials*, vol. 169, no. 1–3, pp. 933–940, 2009.

[27] R. K. Wahi, W. W. Yu, Y. Liu et al., "Photodegradation of Congo Red catalyzed by nanosized TiO_2," *Journal of Molecular Catalysis A*, vol. 242, no. 1-2, pp. 48–56, 2005.

[28] A. B. Sifontes, G. Gonzalez, J. L. Ochoa, L. M. Tovar, T. Zoltan, and E. Cañizales, "Chitosan as template for the synthesis of ceria nanoparticles," *Materials Research Bulletin*, vol. 46, no. 11, pp. 1794–1799, 2011.

[29] D. Valechha, S. Lokhande, M. Klementova, J. Subrt, S. Rayalu, and N. Labhsetwar, "Study of nano-structured ceria for catalytic CO oxidation," *Journal of Materials Chemistry*, vol. 21, no. 11, pp. 3718–3725, 2011.

[30] E. P. Barrett, L. G. Joyner, and P. P. Halenda, "The determination of pore volume and area distributions in porous substances. I. Computations from nitrogen isotherms," *Journal of the American Chemical Society*, vol. 73, no. 1, pp. 373–380, 1951.

[31] V. K. Ivanov, A. E. Baranchikov, O. S. Polezhaeva, G. P. Kopitsa, and Y. D. Tret'yakov, "Oxygen nonstoichiometry of nanocrystalline ceria," *Russian Journal of Inorganic Chemistry*, vol. 55, no. 3, pp. 325–327, 2010, Translation of Zhurnal Neorganicheskoi Khimii.

[32] K. Madhusudan Reddy, C. V. Gopal Reddy, and S. V. Manorama, "Preparation, characterization, and spectral studies on nanocrystalline anatase TiO_2," *Journal of Solid State Chemistry*, vol. 158, no. 2, pp. 180–186, 2001.

[33] S. Damyanova, C. A. Perez, M. Schmal, and J. M. C. Bueno, "Characterization of ceria-coated alumina carrier," *Applied Catalysis A*, vol. 234, no. 1-2, pp. 271–282, 2002.

[34] A. Bensalem, J. C. Muller, and F. Bozon-Verduraz, "Faraday communications. From bulk CeO_2 to supported cerium-oxygen clusters: a diffuse reflectance approach," *Journal of the Chemical Society, Faraday Transactions*, vol. 88, no. 1, pp. 153–154, 1992.

[35] F. Yakuphanoglu and M. Arslan, "The fundamental absorption edge and optical constants of some charge transfer compounds," *Optical Materials*, vol. 27, no. 1, pp. 29–37, 2004.

[36] A. Corma, P. Atienzar, H. García, and J.-Y. Chane-Ching, "Hierarchically mesostructured doped CeO_2 with potential for solar-cell use," *Nature Materials*, vol. 3, no. 6, pp. 394–397, 2004.

[37] R. C. R. Neto and M. Schmal, "Synthesis of CeO_2 and $CeZrO_2$ mixed oxide nanostructured catalysts for the iso-syntheses reaction," *Applied Catalysis A*, vol. 450, pp. 131–142, 2013.

[38] S. T. Hussain and A. Siddiqa, "Iron and chromium doped titanium dioxide nanotubes for the degradation of environmental and industrial pollutants," *International Journal of Environmental Science and Technology*, vol. 8, no. 2, pp. 351–362, 2011.

[39] S. Samiee and E. K. Goharshadi, "Effects of different precursors on size and optical properties of ceria nanoparticles prepared by microwave-assisted method," *Materials Research Bulletin*, vol. 47, no. 4, pp. 1089–1095, 2012.

[40] E. K. Goharshadi, S. Samiee, and P. Nancarrow, "Fabrication of cerium oxide nanoparticles: characterization and optical properties," *Journal of Colloid and Interface Science*, vol. 356, no. 2, pp. 473–480, 2011.

[41] J.-J. Miao, H. Wang, Y.-R. Li, J.-M. Zhu, and J.-J. Zhu, "Ultrasonic-induced synthesis of CeO_2 nanotubes," *Journal of Crystal Growth*, vol. 281, no. 2-4, pp. 525–529, 2005.

[42] C. Huang, K. Zhu, M. Qi, Y. Zhuang, and C. Cheng, "Preparation and photocatalytic activity of bicrystal phase TiO_2 nanotubes containing TiO_2-B and anatase," *Journal of Physics and Chemistry of Solids*, vol. 73, no. 6, pp. 757–761, 2012.

[43] N. T. Nolan, *Sol-Gel Synthesis and Characterisation of Novel Metal Oxide Nanomaterials for Photocatalytic Applications*, Dublin Institute of Technology, 2010.

[44] S. W. Bennett and A. A. Keller, "Comparative photoactivity of CeO_2, γ-Fe_2O_3, TiO_2 and ZnO in various aqueous systems," *Applied Catalysis B*, vol. 102, no. 3-4, pp. 600–607, 2011.